

Atomically Sharp Lateral Superlattice Heterojunctions Built-In Nitrogen-Doped Nanoporous Graphene


Maria Tenorio, Cesar Moreno,* Pol Febrer, Jesús Castro-Esteban, Pablo Ordejón, Diego Peña,* Miguel Pruneda,* and Aitor Mugarza*

Nanometer scale lateral heterostructures with atomically sharp band discontinuities can be conceived as the 2D analogues of vertical Van der Waals heterostructures, where pristine properties of each component coexist with interfacial phenomena that result in a variety of exotic quantum phenomena. However, despite considerable advances in the fabrication of lateral heterostructures, controlling their covalent interfaces and band discontinuities with atomic precision, scaling down components and producing periodic, lattice-coherent superlattices still represent major challenges. Here, a synthetic strategy to fabricate nanometer scale, coherent lateral superlattice heterojunctions with atomically sharp band discontinuity is reported. By merging interdigitated arrays of different types of graphene nanoribbons by means of a novel on-surface reaction, superlattices of 1D, and chemically heterogeneous nanoporous junctions are obtained. The latter host subnanometer quantum dipoles and tunneling in-gap states, altogether expected to promote interfacial phenomena such as interribbon excitons or selective photocatalysis.

M. Tenorio, C. Moreno, P. Febrer, P. Ordejón, M. Pruneda, A. Mugarza
Catalan Institute of Nanoscience and Nanotechnology (ICN2)
CSIC and The Barcelona Institute of Science and Technology
Campus UAB, Bellaterra, Barcelona 08193, Spain
E-mail: cesar.moreno@unican.es; miguel.pruneda@icn2.cat;
aitor.mugarza@icn2.cat

C. Moreno
Departamento de Ciencias de la Tierra y Física de la Materia
Condensada
Universidad de Cantabria
Santander 39005, Spain
J. Castro-Esteban, D. Peña
Centro de Investigación en Química Biológica e Materiais Moleculares
(CIQUS)
Departamento de Química Orgánica
Universidade de Santiago de Compostela
Santiago de Compostela 15782, Spain
E-mail: diego.pena@usc.es

A. Mugarza
ICREA Institució Catalana de Recerca i Estudis Avançats
Lluís Companys 23, Barcelona 08010, Spain

 The ORCID identification number(s) for the author(s) of this article can be found under <https://doi.org/10.1002/adma.202110099>.

© 2022 The Authors. Advanced Materials published by Wiley-VCH GmbH. This is an open access article under the terms of the Creative Commons Attribution-NonCommercial-NoDerivs License, which permits use and distribution in any medium, provided the original work is properly cited, the use is non-commercial and no modifications or adaptations are made.

DOI: 10.1002/adma.202110099

1. Introduction

Lateral heterostructures combining 2D materials with distinct properties on a covalently bonded, one-atom thick layer have been realized by following several in-situ^[1–4] and prepatterning^[5] methods. However, despite the plethora of new 2D materials available, their combination in lateral heterostructures is severely limited by the lack of epitaxial matching and the chemical stability at the interface.^[3] Besides, although methods to fabricate superlattice heterojunctions have already been proposed,^[2,5] scaling them to the nanoscale and with atomic precision is beyond their limit.

A natural solution for the aforementioned challenges can be found in the bottom-up, on-surface synthesis of gra-

phene-based nanostructures.^[6] Following this method, molecular precursors of different structure^[7–12] and chemical composition^[13–21] can be polymerized to form heterocomponents with tailor designed properties, yet following the graphene backbone structure that leads to chemically stable, epitaxial, and covalent interfaces. In one dimension, different types of graphene-based heterojunctions have been realized by codeposition of two molecular building blocks,^[22–25] or post-synthesis chemical transformation of functional groups.^[26,27] These strategies, however, albeit defining each component with atomic precision, lead to either single or randomly distributed heterojunctions, and are hard to be extrapolated to 2D structures. Moreover, despite the atomic sharpness of the interface structure, the charge redistribution and corresponding band discontinuity gradually evolve within several atomic sites across the junction,^[22,23] limiting the downscalability of superlattices or multijunctions.^[27]

Extending a recently proposed on-surface method to synthesize nanoporous graphene (NPG)^[28] to a two-component sequential growth procedure, we have devised a strategy to assemble 2D lateral heterojunctions, where the component size, interface, and band discontinuity are all designed with atomic precision. The heterostructure can be likewise perceived as a hybrid nanoporous graphene (h-NPG) with a chemically heterogeneous pore structure. The key ingredient to achieve this is a double templating effect that guides the synthesis of each of the components. The first component is a graphene nanoribbon (GNR1) that grows in parallel arrays guided by the template provided by the substrate.^[29] In a second step, the GNR1 array

acts as a dynamic template, defining reactor nanochannels for the synthesis of the second nanoribbon component (GNR2), and fusing with the latter to form $[\text{GNR1-GNR2}]_n$ lateral superlattice heterojunctions. The localization of pyrimidine groups at the edges of GNR2, together with the particular interribbon coupling geometry, results in an overall nanoporous graphene structure where the chemical heterogeneity is introduced with atomic precision at the pore edges.

In contrast to the random distribution of heterojunctions obtained by the longitudinal assembly of codeposited 1D GNR components, our interdigitation strategy enables the formation of atomically precise 2D superlattice heterostructures. On the other hand, the correlated subnanometer localization of dipolar charges and the single C–C bond band discontinuity, together with the localization of frontier bands at the backbone of the nanoribbons, facilitate the scaling of the superlattice period down to 1 nm, a scale so far inaccessible to both the on-surface synthesis of graphene nanostructures and the sequential growth strategy used for 2D materials. The resulting lateral superlattice heterostructures can therefore be conceived as the 2D analogues of the vertical heterostructures, where a few

atom size components with well-defined pristine properties can coexist with emergent interfacial quantum properties.

2. On-Surface Synthesis of the Nanoporous Graphene

The main steps of the process are summarized in **Figure 1**. The first component, GNR1, is the 7-13-AGNR that can be synthesized on an Au(111) surface using 10,10'-dibromo-2,2'-diphenyl-9,9'-bianthracene (**1**), and following the widely used two-step Ullmann polymerization and cyclodehydrogenation (CDH) reaction sequence.^[10,28,29] The corresponding onsets for the two thermally induced reactions are $T_1 = 200$ °C and $T_2 = 400$ °C, respectively. As previously reported, the potential grid formed by the herringbone reconstruction of the Au(111) surface guides the synthesis of this GNR forming periodic arrays.^[29] Three different periods can be obtained depending on the coverage, $d_1 = 7.8$ nm, $d_2 = 3.8$ nm, and $d_3 = 1.9$ nm for 0.5 ML, 0.75 ML, and 1 ML, respectively (1 ML corresponds to the saturation of the d_3 phase by definition). The optimal

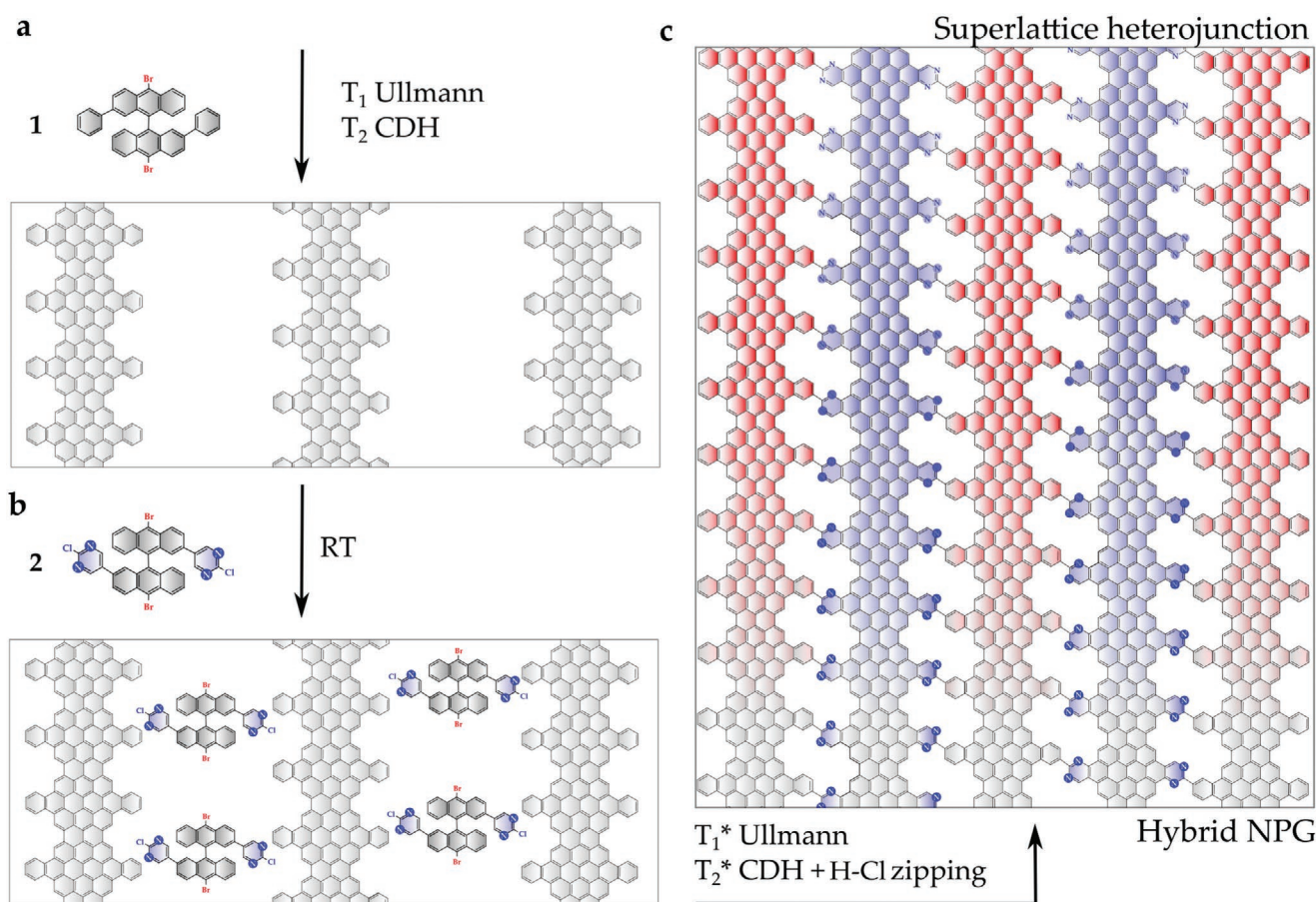


Figure 1. Schematic illustration of the bottom-up fabrication of the superlattice heterojunction built-in a h-NPG. a) GNR1 is synthesized by depositing precursor **1** on Au(111) at room temperature and following the Ullmann polymerization and cyclodehydrogenation (CDH) steps at $T_1 = 200$ °C and $T_2 = 400$ °C, respectively, as reported in Ref. [28]. The ribbons form a 1D array using the herringbone reconstruction of the Au(111) surface as template (see Ref. [29]). b) The GNR1 array serves as a second template to host precursor **2** on the empty Au(111) tracks and guide the synthesis of GNR2. Ullmann polymerization at $T_1^* = 150$ °C, and a simultaneous CDH of poly-**2** into GNR2 and the unprecedented interribbon H–Cl zipping at $T_2^* = 300$ °C lead to a hybrid nanoporous graphene with heterogeneous pore structure and a built-in $[\text{GNR1-GNR2}]_n$ superlattice heterojunction (c).

GNR1 coverage in order to maximize the area of the final h-NPG is determined by the intercalation of precursor 2, which imposes a superlattice periodicity of 2.5 nm before shrinking into the covalently fused h-NPG (see Figure S6, Supporting Information, and discussion below). This average periodicity corresponds to a GNR1 coverage of 0.76 ML. We therefore use GNR1 arrays of densities close to this value for the synthesis of the second component.

For the second component we designed and synthesized 10,10'-dibromo-2,2'-bis(2-chloropyrimidin-5-yl)-9,9'-bianthracene (2), a pyrimidine-substituted bianthracene derivative (details of the monomer synthesis in Experimental Section and Figures S1–S5, Supporting Information). This GNR precursor, being isostructural to 1, bears two important differences: the pyrimidine rings that substitute the phenyls of 1, and the introduction of chlorine atoms in these lateral rings. The pyrimidine introduces chemical heterogeneity to the nanopores, and is expected to modify the electronic band structure of the final GNR2, and consequently of the whole h-NPG. Pyrimidinic N is an isoelectronic substitution that does not introduce additional charges, but its higher affinity results in a local charge accumulation and the corresponding inductive band shift.^[23,30] (see Figure S12, Supporting Information). The role of the chlorine substituents, on the other hand, is to reduce the temperature of the final interribbon lateral cross-coupling in order to assure the survival of the pyrimidine group throughout all the reaction sequence. We do that by substituting the dehydrogenative C–C coupling that requires temperatures of ≈ 450 °C,^[28] high enough to cleave or decompose edge functional groups,^[20,21] by a H–Cl zipping mechanism that emulates the recently reported H–F zipping and can already be triggered at the CDH reaction temperature of 300 °C.^[31,32] This reduction of 100 °C, as compared to the H–F zipping observed on the same surface, is crucial for the synthesis of heterogeneous structures as the one demonstrated in this work, since most heterogeneous moieties cannot withstand the 400 °C needed for the H–F zipping.^[19,20] We envision that this temperature reduction can also be crucial to promote the synthesis of covalent nanostructures on less reactive insulator surfaces, as recently demonstrated by using the H–F zipping.^[31]

The scanning tunneling microscopy (STM) image of Figure 2a shows that precursor 2 deposited at room temperature already intercalate in the interribbon channels (see Figure S6, Supporting Information, for more details). By annealing to $T_1^* = 150$ °C, precursor 2 undergoes Ullmann polymerization, exhibiting the characteristic chain of alternating lobes that can be seen in Figure 2b.^[10] Besides some marginal regions where short, meandering poly-2 chains cluster (see Figure S7, Supporting Information), the surface is covered with an interdigitated [GNR1-(poly-2)]_n superlattice. The longer, straight, poly-2 chains in the interdigitated region suggest that the reactor nanochannels provided by the GNR1 array can be employed as a general strategy to assist polymerization of precursors that lead to undesired intermolecular interactions on a 2D template, as is the case of many functionalized molecules.^[33] The single periodicity of 2.5 nm measured by STM for the interdigitated superlattice indicates that GNR1-(poly-2) interactions unpin the GNR1 superlattice from the herringbone template (see Figure S6, Supporting Information).

The presence of a chlorine atom on each pyrimidine ring not only reduces the interribbon cross-coupling, but also the internal CDH of poly-2 into GNR2, which are triggered simultaneously at $T_2^* = 300$ °C (Figure 2c). The periodicity of 1.7 nm measured for the resulting interdigitated [GNR1-GNR2] superlattice patches are close to the nominal value of 1.6 nm of the covalently bonded GNR array that form h-NPG (see Figure S6, Supporting Information). Although most of the patches we find consist of 4–5 coupled GNRs, we can find larger patches with up to 9–10 coupled GNRs (see Figure S8, Supporting Information). Bond resolved (BR-) STM images acquired with a CO-functionalized tip as the one shown in Figure 2d demonstrate the coupling of adjacent GNRs, and enable the direct visualization of the chemically heterogeneous nanopores defining the junctions by revealing clear chemical contrast between the bridging units of the two components, as illustrated by the line profiles of Figure 2d.

3. Electronic Characterization of the Superlattice Heterostructure

The interdigitated GNRs defining the h-NPG imprint a staggered (type II) superlattice heterojunction band structure with atomically sharp discontinuities. The band gaps and discontinuities can be directly probed by measuring the local density of states (LDOS) within each type of nanoribbon by scanning tunneling spectroscopy (STS). The dI/dV spectra of Figure 3a reveal a pair of peaks that can be assigned to the valence band maxima (VBM) and conduction band minima (CBM) of each component, aided by the identification of features related to these states in corresponding dI/dV maps (see Figure S11, Supporting Information). Our analysis leads to similar band gaps of 1.25 eV for GNR1 and 1.47 eV for GNR2, with the VBM and CBM, respectively, downshifted by 0.41 and 0.19 eV for GNR2, as expected for the N-doped component.^[23,30] The magnitude of the valence and conduction band offsets is well captured by a similar shift of 0.42/0.41 eV found for the VBM/CBM in the density functional theory (DFT) band structure shown in Figure 3c. We attribute the differences found in the experimental band gaps to the different degree of screening of substrate electrons in each case, which can be due to a more effective decoupling of the N-doped GNR, as recently found in zigzag GNRs.^[34]

This substantial band discontinuity exerts an effective confinement of the frontier bands of each heterocomponent, as can be visualized in the constant current dI/dV maps and constant height LDOS cuts shown in Figure 3d. However, the corresponding wave functions of the interdigitated components do not completely vanish at adjacent GNRs (Figure 3d bottom). In particular, the VBM of GNR1 and CBM of GNR2 extend across adjacent GNRs as faint diagonal stripes, even if these are forbidden gap regions. We attribute it to the tunneling of these states across the junction, which can also be perceived in the DOS of Figure 3c for a high enough amplification (dashed lines). The tunneling contributions are not detected in the dI/dV and LDOS maps due to the fact that their weak signal is further attenuated by the faster decay of the wave function into the vacuum at the backbone of GNRs.^[35]

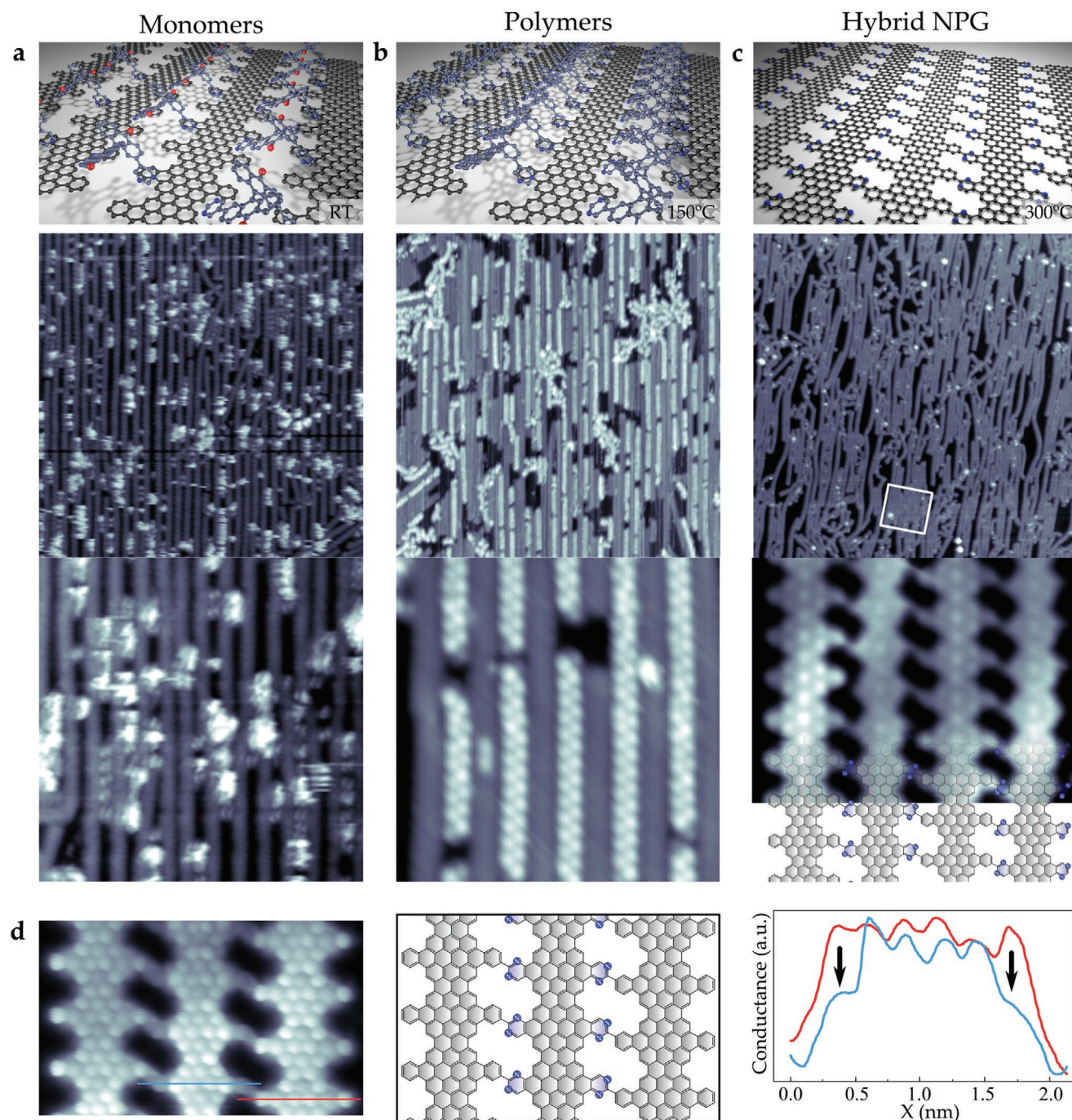


Figure 2. STM characterization of the on-surface synthesis of h-NPG. a–c) Synthesis of GNR2 within the GNR1 array. The STM topographic images show: a) intercalated monomers of 2 after deposition at room temperature. b) Formation of poly-2 chains interdigitated within the GNR1 array after annealing at $T_1^* = 150$ °C. c) Simultaneous cyclodehydrogenation (CDH) and interribbon cross-coupling by H–Cl zipping, which leads to the $[\text{GNR1-GNR2}]_n$ superlattice heterostructure, after annealing at $T_2^* = 300$ °C. Top/bottom images represent large and small scale areas, not necessarily of the same region. d) BR-STM of a $[\text{GNR1-GNR2-GNR1}]$ triplet obtained with a CO-functionalized tip unveiling clear chemical contrast between the bridging pyrimidine rings of the N-doped GNR2 (center ribbon) and the benzene rings of the undoped GNR1 (side ribbons). The significantly lower contrast of the pyrimidine rings is clearly visualized at the transversal profiles obtained at the lines marked in the STM image. All imaging parameters are detailed in Table S1, Supporting Information.

In-gap tunneling states have been predicted to exist in well-defined heterojunctions with an atomically sharp potential step.^[36] In a more detailed analysis of our experimental and theoretical data, we find evidences for both, the atomically

sharp potential steps and the presence of tunneling states. Figure 3b shows a series of constant current dI/dV spectra acquired across a GNR1-GNR2 interface. Here, the CB+1 maxima exhibit a sharp discontinuity at the interface within

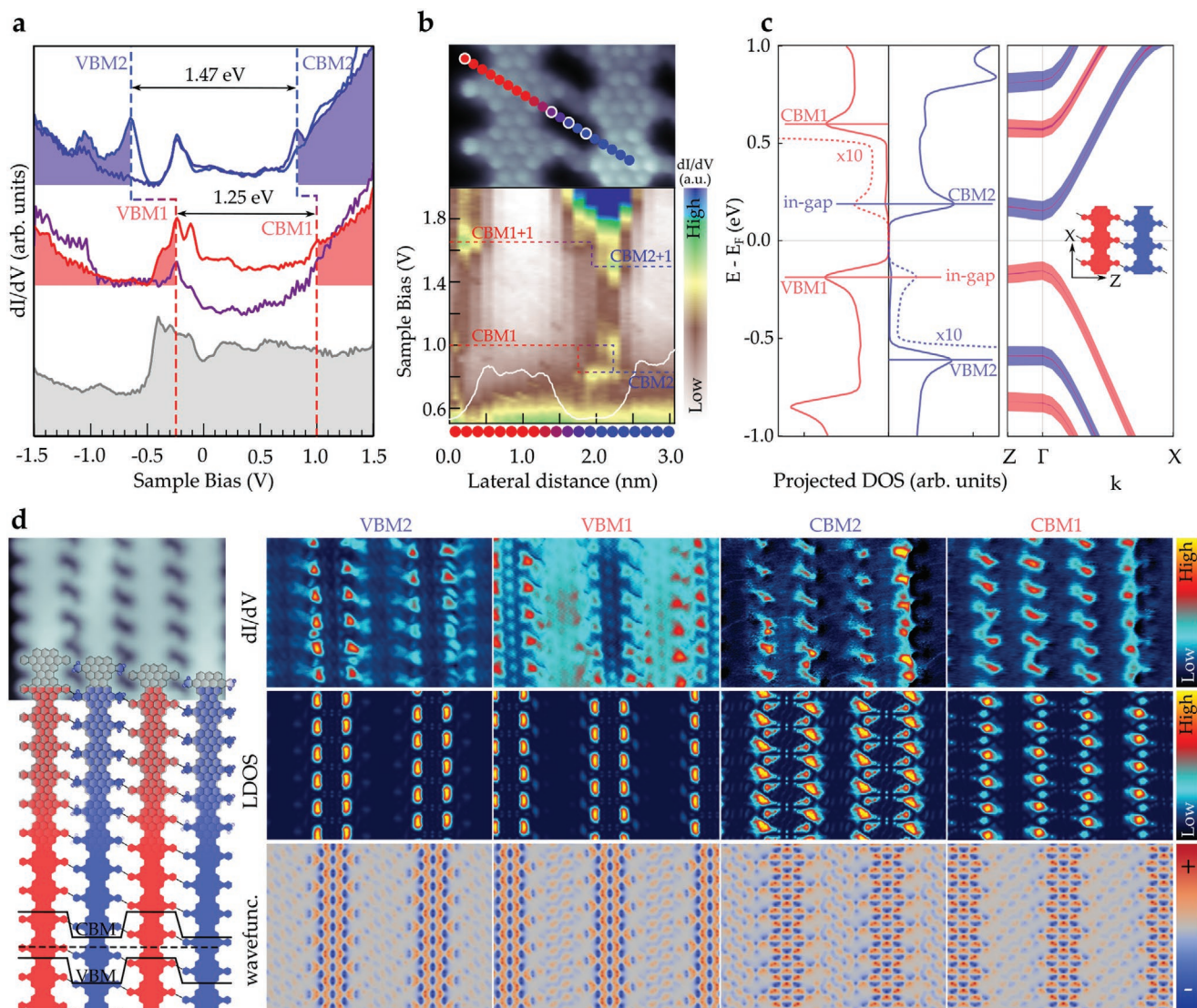


Figure 3. Electronic band structure of h-NPG. a) Representative dI/dV spectra of GNR1 and GNR2, where the VBM and CBM are marked with dashed vertical lines (positions of the selected spectra are highlighted with white outline in the series of Figure 3b). The corresponding band gap is indicated. A spectrum acquired on Au(111) is included as reference (shadowed grey line). b) Color plot of a series of constant current dI/dV spectra acquired along a line that crosses a GNR1-GNR2 pair within the triplet shown in Figure 2d. The topographic profile along the spectroscopic series is overlaid as white line. c) DFT band structure of the $[GNR1-GNR2]_n$ superlattice. Colored fat bands represent the projection onto GNR1 (red) and GNR2 (blue). The DOS of each heterocomponent is added on the left. d) Constant current dI/dV maps and constant height LDOS cuts at the height of $h = 0.3$ nm. Represented wavefunctions have been integrated from the nodal plane ($y = 0$) to infinite. Red/blue colors correspond to \pm values. The topographic images where the maps were acquired are shown at the left, overlapped with a schematic illustration that includes the superlattice band offsets. All STS parameters are detailed in Table S1, Supporting Information.

the step size of 0.15 nm, a single C–C bond, used in the spectroscopic series. This value is significantly smaller than the already narrow band bending region found in 0D heterojunctions in graphene nanoribbons.^[23,26] The CBM of both components also show constant energy levels, separated by ≈ 0.2 eV, but in this case they interpenetrate across the interface, which we tentatively attribute to tunneling. The decay of the tunneling tail can be better studied in simulated log scale LDOS scans, as the one shown in Figure 4a for a [GNR1-GNR2-GNR1] triplet. The finite segment allows us to simultaneously visualize the decay of CBM states of GNR2 within the GNR1 region, and

the strong overlap of the tails of the VBM of GNR1 coming from each heterojunction into the central GNR2 region. This overlap is the origin of the “stripes” that connect the VBM/CBM wave functions in the periodic superlattice of Figure 3d. In order to study the evolution of the overlap with the period of the superlattice, in Figure 4b we analyze squared wave function profiles for $[(GNR1)_m-(GNR2)_m]_n$ heterojunctions of different periodicity $w = m \times d$ ($d = 1.6$ nm is the inter-ribbon distance in the superlattice). For the superlattice that we synthesized, the $m = 1$, a small but finite overlap of the in-gap tails within the single ribbon components (blue line sections) can be clearly

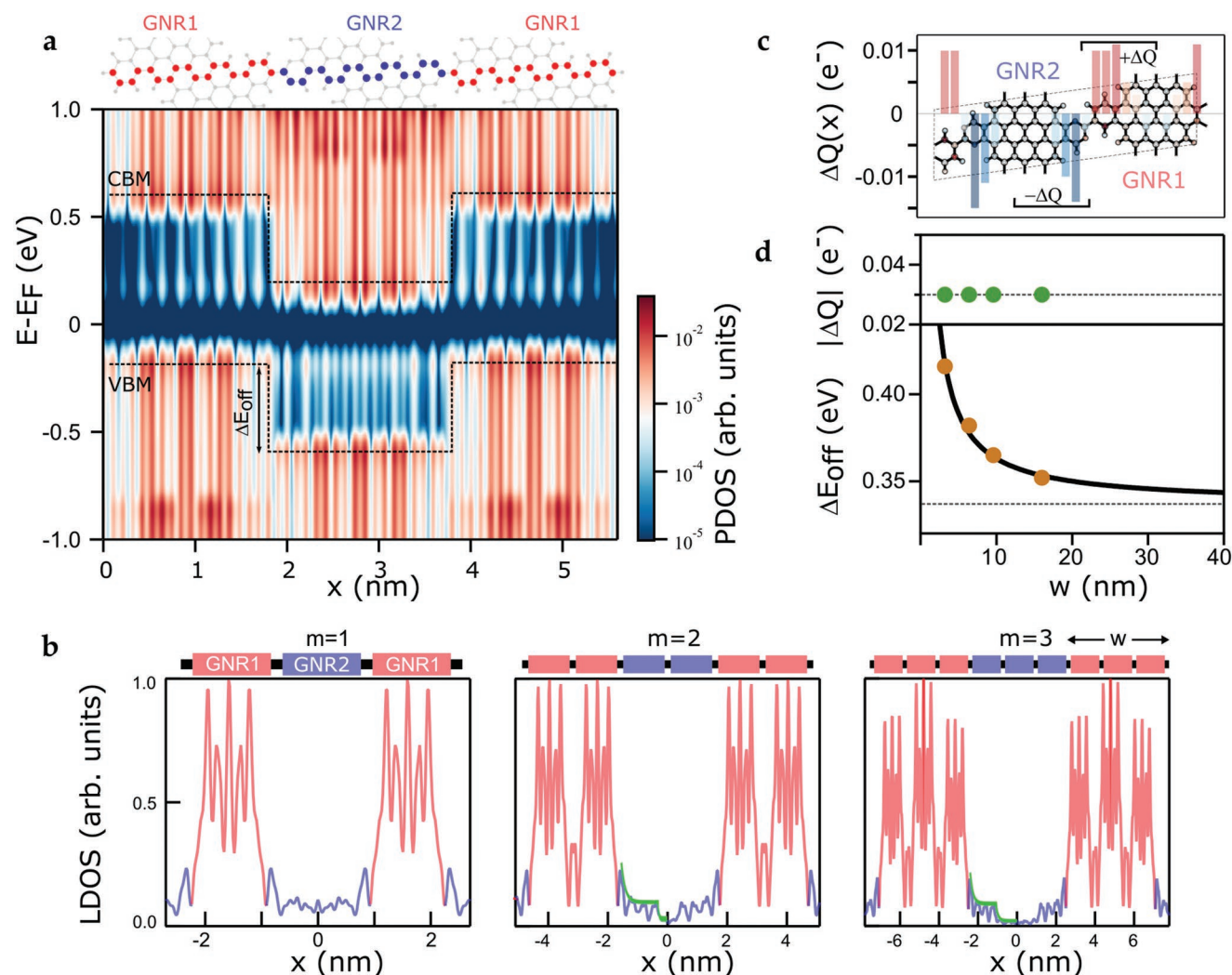


Figure 4. In-gap states and quantum dipoles. a) Simulated LDOS scan across a GNR1-GNR2-GNR1 triplet. The path of the scan line is indicated with colored atoms on the schematic on top. The color plot is in log scale to enhance in-gap states within the gap. b) Profiles of the square of the wave functions of the VBM of GNR1 averaged along the ribbon direction for $m = 1-3$ superlattices, showing the evolution of the decaying in-gap tail at GNR2. The green line is an envelope guideline. c) Hirshfeld charge difference with respect to individual GNR1 and GNR2, averaged in columns along the ribbon direction. The sum over half segments of the ribbons defines the dipolar charge $\pm\Delta Q$. The charge difference at each atom is also depicted in red/blue (+/-) color scale. d) Evolution of the dipolar charge and band offset with the superlattice period, the latter measured at the VBM. The band offset data is fitted with the inverse law model of Ref. [37]. The dashed line in the top graph refers to dipolar charge of the $m = 1$ superlattice, and in the bottom graph to the band shift of the infinite superlattice.

perceived. For superlattices with wider heterocomponents ($m > 1$), the distance between junctions is enough to prevent any significant overlap, leading to an effective disconnection of the interdigitated GNRs (see Figure S10, Supporting Information, for corresponding 2D wave functions plots). Notably, the bridges that couple GNR2 units introduce step discontinuities that further attenuate the decay. This is evident for $m = 3$, where the in-gap state abruptly decays to negligible values when entering the central GNR2 unit (follow guiding green line sections in Figure 4b).

Interfacial in-gap states are inherently associated with a charge redistribution, which can induce significant band realignment.^[36] Unlike conventional bulk heterostructures, the interfacial dipole potential of 1D (lateral) heterojunctions decays logarithmically with the distance from the junction. In

superlattice heterostructures with periodicity w larger than the interfacial dipole, the potential decays as $1/w$. Consequently, for periods smaller than the characteristic decay length, which can be as large as 30 nm for semiconductor heterojunctions such as MoS_2/WS_2 ,^[37] the band offset is size-dependent. In narrow superlattices the interaction between adjacent dipoles can also lead to charge redistributions that induce additional shifts.^[27] These two factors demand an accurate control on the superlattice quality for a homogenous, well-controlled band offset. In order to discern the different mechanisms for band realignment, we tracked the evolution of both the dipole charge and band offset with respect to the superlattice period. Figure 4d shows that the dipole charge $|\Delta Q|$, as obtained from the Hirshfeld charge difference integrated in half segment of each type of ribbon (see Figure 4c), remains nearly constant down to the

narrowest superlattice $m = 1$. This is a further manifestation of the strong localization of the quantum dipoles that characterize these heterojunctions, estimated to be within two carbon bond-lengths from the interface, well below the narrowest superlattice period of 1.6 nm. This result is in contrast with the significant charge redistribution found for 0D heterojunctions of similar width within single GNRs.^[27] Confirming the rigid dipole scenario, the band realignment evolution follows the inverse scaling down to $m = 1$ (see Figure 4d). The fit of the data results in a decay length of 78 nm, measured as the period where the band offset deviates 10% from the asymptotic value of 0.34 eV of the infinite superlattice.

4. Conclusions

In conclusion, our synthetic method provides a route to realize lateral superlattice heterojunctions with an atomically sharp step potential and nanometer scale period that is well below the screening length of the interfacial dipole. The band offset is controlled by the atomic scale design of the components and the strong localization of the interfacial quantum dipoles. The sharp band discontinuity together with the presence of tunneling states at both sides of the junction is expected to promote interribbon excitons, the 1D analogue^[38] of interlayer excitons in vertical heterostructures,^[39–43] as well as efficient charge separation that can be relevant for optoelectronics and excitonic solar cells.^[44] The coexistence of a type II superlattice band structure with heterogeneous nanopores at the junction makes this graphene-based nanomaterial particularly attractive for photocatalytic applications such as water splitting.^[45] Furthermore, the N-doped nanopores of the one atom thick hybrid layer could be relevant for membrane applications such as selective ion sieving.^[46]

5. Experimental Section

Synthesis of the Molecular Precursors by Means of Solution Chemistry (General Methods): All reactions were carried out under argon using oven-dried glassware. TLC was performed on Merck silica gel 60 F₂₅₄; chromatograms were visualized with UV light (254 and 360 nm). Flash column chromatography was performed on Merck silica gel 60 (ASTM 230–400 mesh). ¹H and ¹³C NMR spectra were recorded at 300 and 75 MHz or 500 and 125 MHz (Varian Mercury 300 or Bruker DPX-500 instruments), respectively. APCI spectra were determined on a Bruker Microtof instrument. A detailed description of the synthetic route for each molecular precursor can be found in the Supporting Information.

Sample Preparation: The Au(111) single crystal was prepared by repeated sputter-anneal cycles using Ar⁺ ions at an energy of 1 keV and annealing to 470 °C. The precursor 1 was sublimated at 270 °C with a deposition rate of 0.1 monolayer/min and with the Au(111) held at 200 °C, whereas precursor 2 was sublimated at the temperature of 320 °C with a deposition rate of 0.006 ML min⁻¹ and the Au(111) substrate at room temperature, both from the same commercial Dodecon OMBE fourfold Knudsen cell. The sample temperature was measured by using a thermocouple directly in contact with the sample. The base pressure during evaporation was below 1×10^{-9} mbar.

Scanning Tunneling Microscopy and Spectroscopy: The images of Figure 2 (except c Bottom and d) were acquired in constant current (CC) mode and without any intentional functionalization of the tip apex. Images in Figures 2c, bottom, and 2d were acquired in constant height (CH) mode, and with a CO-functionalized tip to perform bond-resolved

STM (BR-STM). All conditions for image acquisition are summarized in Table S1, Supporting Information.

For the tip functionalization, CO molecules were first introduced on the Au surface by dosing the cryostat with CO gas at a pressure of 5×10^{-7} mbar for 30 s in a temperature range from 5 to 15 K. The CO was then picked up by the tip by applying pulses of 2.5 V at random positions or by gentle tip indentations on the Au surface until the resolution was suddenly improved. The higher resolution of these tips are related to dynamic effects in the CO-metallic tip junction as it interacts with the atoms beneath.^[47]

dI/dV conductance maps in Figure 3 were acquired in CC mode with a standard metallic tip using a lock-in technique. All the parameters are listed in Table S1, Supporting Information.

The I–V conditions of the STM images of Figures S6 and S7 are listed in Table S2, Supporting Information.

DFT Calculations: All the electronic structure analysis in this work has been performed with DFT calculations using the SIESTA code.^[48–50] For the simulations the authors used the PBE form of the GGA exchange-correlation functional, with an optimized DZP basis set with diffuse orbitals for C and H atoms and the default DZP basis set for N with an energy shift of 0.01 Ry. The structures were relaxed up to a force tolerance of 0.01 eV Å⁻¹. To avoid interactions between periodic replicas of the 2D layer, a large vacuum region ≈ 35 nm was included in the simulation box. The mesh cut-off was set to 400 Ry. To sample the reciprocal space, they used a Monkhorst–Pack grid with 30 k points in the longitudinal (ribbon) direction and at least 3 k points in the transversal direction. Post processing of the results was done using the sisl python package.^[51]

Theory Calculations Processing: PDOS curves in Figure 3c have been obtained with a $60 \times 30 \times 1$ k point sampling and smoothed out using a Gaussian with $\sigma = 0.05$ eV. All the wave functions displayed in this work were integrated over the Z axis from the position of the NPG sheet to the vacuum (only on one side of the monolayer in order to keep phase information). The longitudinal ribbon direction (Y) is also integrated whenever the wave function is plotted along the superlattice axis (X) only. In the case of the LDOS displayed in Figure 3d, the authors only considered a small range from 3 to 3.5 Å above the NPG sheet to compare with the STM images. For the LDOS in Figure 4a, a Gaussian convolution with $\sigma = 0.1$ eV has been applied to the energy axis to get a smoother visualization. In the analysis of atomic charges, each bar represents the integrated contributions of a “YZ” plane placed at the center of the bar, with each atom contributing to its nearest plane.

Statistical Analysis: Topographic images have only been treated with plane subtraction, rotation, and zooming when necessary, except Figure 2a, top, and Figure S6c (inset), Supporting Information, which have been also smoothed with a 3×3 matrix convolution. Scanning tunneling spectroscopy (STS) spectra from Figure 3a have been averaged with the respective forward and backward spectra, and it has been smoothed by linear interpolation with a total number of 2000 points and 150 nodes. Representative values were selected for the distances between GNRs in the intermediate and final stages in Figure S6, Supporting Information. For the GNRs center-to-center distance, profiles were extracted from images using the WSxM program.^[52]

Supporting Information

Supporting Information is available from the Wiley Online Library or from the author.

Acknowledgements

This research was funded by the CERCA Programme/Generalitat de Catalunya and supported by the Spanish Ministry of Economy and Competitiveness, MINECO (Grant No. SEV-2017-0706), Grants PID2019-107338RB-C65, and PID2019-107338RB-C62, funded by MCIN/AEI/ 10.13039/501100011033, Grant PGC2018-096955-B-C43 funded by

MCIN/AEI/ 10.13039/501100011033 and by “ERDF A way of making Europe”, FLAG-ERA grant LEGOCHIP Projects PCI2019-111890-2 and PCI2019-111933-2 funded by MCIN/AEI /10.13039/501100011033 and cofounded by the European Union, the GenCat (Grant No. 2017SGR1506), the European Union MaX Center of Excellence (EU-H2020 Grant No. 924143), the European Regional Development Fund (ERDF) under the program Interreg V-A España-Francia-Andorra (Grant No. EFA 194/16 TNSI), and Xunta de Galicia (Centro Singular de Investigación de Galicia accreditation 2019–2022, ED431G 2019/03). C.M. was supported by Grant RYC2019-028110-I funded by MICIN/AEI/ 10.13039/501100011033 and by “ESF Investing in your future”. M.T. has been supported by Spanish State Research Agency/FSE (ref. BES-2017-08078, project ref. SEV-2013-0295-17-2). The authors thankfully acknowledge the computer resources at MareNostrum and the technical support provided by Barcelona Supercomputing Center (RES-QCM-2019-1-0051).

Note: The funding acknowledgements were corrected on May 19, 2022, after initial publication online.

Conflict of Interest

The authors declare no conflict of interest.

Author Contributions

D.P. and J.C.-E. designed and synthesized the molecular precursor. M.P., P. O., and P.F. performed the ab-initio calculations. A.M., C.M., and M.T. planned the on-surface synthesis and STM experiments, and analyzed the data. C.M. and M.T. performed the on-surface synthesis and STM measurements. All authors discussed the results and participated in writing the manuscript. M.P. and A.M. directed this research.

Data Availability Statement

The data that support the findings of this study are available from the corresponding author upon reasonable request.

Keywords

2D materials, graphene, lateral heterostructures, nanoarchitectonics, on-surface synthesis, scanning tunneling microscopy

Received: December 11, 2021

Revised: March 18, 2022

Published online: March 25, 2022

- [1] M.-Y. Li, Y. Shi, C.-C. Cheng, L.-S. Lu, Y.-C. Lin, H.-L. Tang, M.-L. Tsai, C.-W. Chu, K.-H. Wei, J.-H. He, W.-H. Chang, K. Suenaga, L.-J. Li, *Science* **2015**, 349, 524.
- [2] S. Xie, L. Tu, Y. Han, L. Huang, K. Kang, K. U. Lao, P. Poddar, C. Park, D. A. Muller, R. A. DiStasio, J. Park, *Science* **2018**, 359, 1131.
- [3] P. K. Sahoo, S. Memaran, Y. Xin, L. Balicas, H. R. Gutiérrez, *Nature* **2018**, 553, 63.
- [4] J. Wang, Z. Li, H. Chen, G. Deng, X. Niu, *Nano-Micro Lett.* **2019**, 11, 48.
- [5] M. Mahjour-Samani, M.-W. Lin, K. Wang, A. R. Lupini, J. Lee, L. Basile, A. Boulesbaa, C. M. Rouleau, A. A. Puzos, I. N. Ivanov, K. Xiao, M. Yoon, D. B. Geohegan, *Nat. Commun.* **2015**, 6, 7749.
- [6] Z. Chen, A. Narita, K. Müllen, *Adv. Mater.* **2020**, 32, 2001893.

- [7] J. Cai, P. Ruffieux, R. Jaafar, M. Bieri, T. Braun, S. Blankenburg, M. Muoth, A. P. Seitsonen, M. Saleh, X. Feng, K. Müllen, R. Fasel, *Nature* **2010**, 466, 470.
- [8] D. G. de Oteyza, A. García-Lekue, M. Vilas-Varela, N. Merino-Díez, E. Carbonell-Sanromà, M. Corso, G. Vasseur, C. Rogero, E. Guitián, J. I. Pascual, J. E. Ortega, Y. Wakayama, D. Peña, *ACS Nano* **2016**, 10, 9000.
- [9] J. Liu, B.-W. Li, Y.-Z. Tan, A. Giannakopoulos, C. Sanchez-Sanchez, D. Beljonne, P. Ruffieux, R. Fasel, X. Feng, K. Müllen, *J. Am. Chem. Soc.* **2015**, 137, 6097.
- [10] C. Moreno, M. Panighel, M. Vilas-Varela, G. Sauthier, M. Tenorio, G. Ceballos, D. Peña, A. Mugarza, *Chem. Mater.* **2019**, 31, 331.
- [11] O. Gröning, S. Wang, X. Yao, C. A. Pignedoli, G. Borin Barin, C. Daniels, A. Cupo, V. Meunier, X. Feng, A. Narita, K. Müllen, P. Ruffieux, R. Fasel, *Nature* **2018**, 560, 209.
- [12] D. J. Rizzo, G. Veber, T. Cao, C. Bronner, T. Chen, F. Zhao, H. Rodríguez, S. G. Louie, M. F. Crommie, F. R. Fischer, *Nature* **2018**, 560, 204.
- [13] S. Kawai, S. Saito, S. Osumi, S. Yamaguchi, A. S. Foster, P. Spijker, E. Meyer, *Nat. Commun.* **2015**, 6, 8098.
- [14] G. D. Nguyen, F. M. Toma, T. Cao, Z. Pedramrazi, C. Chen, D. J. Rizzo, T. Joshi, C. Bronner, Y.-C. Chen, M. Favaro, S. G. Louie, F. R. Fischer, M. F. Crommie, *J. Phys. Chem. C* **2016**, 120, 2684.
- [15] A. Basagni, G. Vasseur, C. A. Pignedoli, M. Vilas-Varela, D. Peña, L. Nicolas, L. Vitali, J. Lobo-Checa, D. G. de Oteyza, F. Sedona, M. Casarin, J. E. Ortega, M. Sambri, *ACS Nano* **2016**, 10, 2644.
- [16] Y. Fu, H. Yang, Y. Gao, L. Huang, R. Berger, J. Liu, H. Lu, Z. Cheng, S. Du, H. Gao, X. Feng, *Angew. Chem., Int. Ed.* **2020**, 59, 8873.
- [17] C. Bronner, S. Stremelau, M. Gille, F. Brauße, A. Haase, S. Hecht, P. Tegeder, *Angew. Chem., Int. Ed.* **2013**, 52, 4422.
- [18] X.-Y. Wang, J. I. Urgel, G. B. Barin, K. Eimre, M. Di Giovannantonio, A. Milani, M. Tommasini, C. A. Pignedoli, P. Ruffieux, X. Feng, R. Fasel, K. Müllen, A. Narita, *J. Am. Chem. Soc.* **2018**, 9104.
- [19] E. Carbonell-Sanromà, J. Hieulle, M. Vilas-Varela, P. Brandimarte, M. Iraola, A. Barragán, J. Li, M. Abadia, M. Corso, D. Sánchez-Portal, D. Peña, J. I. Pascual, *ACS Nano* **2017**, 11, 7355.
- [20] J. Li, P. Brandimarte, M. Vilas-Varela, N. Merino-Díez, C. Moreno, A. Mugarza, J. S. Mollejo, D. Sánchez-Portal, D. Garcia de Oteyza, M. Corso, A. Garcia-Lekue, D. Peña, J. I. Pascual, *ACS Nano* **2020**, 14, 1895.
- [21] M. Panighel, S. Quiroga, P. Brandimarte, C. Moreno, A. Garcia-Lekue, M. Vilas-Varela, D. Rey, G. Sauthier, G. Ceballos, D. Peña, A. Mugarza, *ACS Nano* **2020**, 14, 11120.
- [22] Y.-C. Chen, T. Cao, C. Chen, Z. Pedramrazi, D. Haberer, D. G. de Oteyza, F. R. Fischer, S. G. Louie, M. F. Crommie, *Nat. Nanotechnol.* **2015**, 10, 156.
- [23] J. Cai, C. A. Pignedoli, L. Talirz, P. Ruffieux, H. Söde, L. Liang, V. Meunier, R. Berger, R. Li, X. Feng, K. Müllen, R. Fasel, *Nat. Nanotechnol.* **2014**, 9, 896.
- [24] P. H. Jacobse, A. Kimouche, T. Gebraad, M. M. Ervasti, J. M. Thijssen, P. Liljeroth, I. Swart, *Nat. Commun.* **2017**, 8, 119.
- [25] C. Bronner, R. A. Durr, D. J. Rizzo, Y.-L. Lee, T. Marangoni, A. M. Kalayjian, H. Rodriguez, W. Zhao, S. G. Louie, F. R. Fischer, M. F. Crommie, *ACS Nano* **2018**, 12, 2193.
- [26] G. D. Nguyen, H.-Z. Tsai, A. A. Omrani, T. Marangoni, M. Wu, D. J. Rizzo, G. F. Rodgers, R. R. Cloke, R. A. Durr, Y. Sakai, F. Liou, A. S. Aikawa, J. R. Chelikowsky, S. G. Louie, F. R. Fischer, M. F. Crommie, *Nat. Nanotechnol.* **2017**, 12, 1077.
- [27] D. J. Rizzo, M. Wu, H.-Z. Tsai, T. Marangoni, R. A. Durr, A. A. Omrani, F. Liou, C. Bronner, T. Joshi, G. D. Nguyen, G. F. Rodgers, W.-W. Choi, J. H. Jørgensen, F. R. Fischer, S. G. Louie, M. F. Crommie, *Nano Lett.* **2019**, 19, 3221.
- [28] C. Moreno, M. Vilas-Varela, B. Kretz, A. Garcia-Lekue, M. V. Costache, M. Paradinas, M. Panighel, G. Ceballos, S. O. Valenzuela, D. Peña, A. Mugarza, *Science* **2018**, 360, 199.

- [29] C. Moreno, M. Paradinas, M. Vilas-Varela, M. Panighel, G. Ceballos, D. Peña, A. Mugarza, *Chem. Commun.* **2018**, 54, 9402.
- [30] R. A. Durr, D. Haberer, Y.-L. Lee, R. Blackwell, A. M. Kalayjian, T. Marangoni, J. Ihm, S. G. Louie, F. R. Fischer, *J. Am. Chem. Soc.* **2018**, 140, 807.
- [31] M. Kolmer, R. Zuzak, A. K. Steiner, L. Zajac, M. Englund, S. Godlewski, M. Szymanski, K. Amsharov, *Science* **2019**, 363, 57.
- [32] Q. Fan, L. Yan, M. W. Tripp, O. Krejčí, S. Dimosthenous, S. R. Kachel, M. Chen, A. S. Foster, U. Koert, P. Liljeroth, J. M. Gottfried, *Science* **2021**, 372, 852.
- [33] M. Liu, M. Liu, L. She, Z. Zha, J. Pan, S. Li, T. Li, Y. He, Z. Cai, J. Wang, Y. Zheng, X. Qiu, D. Zhong, *Nat. Commun.* **2017**, 8, 14924.
- [34] R. E. Blackwell, F. Zhao, E. Brooks, J. Zhu, I. Piskun, S. Wang, A. Delgado, Y.-L. Lee, S. G. Louie, F. R. Fischer, *Nature* **2021**, 600, 647.
- [35] H. Söde, L. Talirz, O. Gröning, C. A. Pignedoli, R. Berger, X. Feng, K. Müllen, R. Fasel, P. Ruffieux, *Phys. Rev. B* **2015**, 91, 045429.
- [36] J. Tersoff, *Phys. Rev. B* **1984**, 30, 4874.
- [37] J. Zhang, W. Xie, J. Zhao, S. Zhang, *2D Mater.* **2017**, 4, 015038.
- [38] K. W. Lau, Z. G. Calvin, H. Yu, W. Yao, *Phys. Rev. B* **2018**, 98, 115427.
- [39] Y. Jiang, S. Chen, W. Zheng, B. Zheng, A. Pan, *Light: Sci. Appl.* **2021**, 10, 72.
- [40] K. Tran, G. Moody, F. Wu, X. Lu, J. Choi, K. Kim, A. Rai, D. A. Sanchez, J. Quan, A. Singh, J. Embley, A. Zepeda, M. Campbell, T. Autry, T. Taniguchi, K. Watanabe, N. Lu, S. K. Banerjee, K. L. Silverman, S. Kim, E. Tutuc, L. Yang, A. H. MacDonald, X. Li, *Nature* **2019**, 567, 71.
- [41] C. Jin, E. C. Regan, A. Yan, M. Iqbal Bakti Utama, D. Wang, S. Zhao, Y. Qin, S. Yang, Z. Zheng, S. Shi, K. Watanabe, T. Taniguchi, S. Tongay, A. Zettl, F. Wang, *Nature* **2019**, 567, 76.
- [42] E. M. Alexeev, D. A. Ruiz-Tijerina, M. Danovich, M. J. Hamer, D. J. Terry, P. K. Nayak, S. Ahn, S. Pak, J. Lee, J. I. Sohn, M. R. Molas, M. Koperski, K. Watanabe, T. Taniguchi, K. S. Novoselov, R. V. Gorbachev, H. S. Shin, V. I. Fal'ko, A. I. Tartakovskii, *Nature* **2019**, 567, 81.
- [43] Z. Wang, D. A. Rhodes, K. Watanabe, T. Taniguchi, J. C. Hone, J. Shan, K. F. Mak, *Nature* **2019**, 574, 76.
- [44] L. Liang, V. Meunier, *J. Phys. Chem. C* **2015**, 119, 775.
- [45] S. Wang, J. Zhang, B. Li, H. Sun, S. Wang, *Energy Fuels* **2021**, 35, 6504.
- [46] K. Sint, B. Wang, P. Král, *J. Am. Chem. Soc.* **2008**, 130, 16448.
- [47] P. Jelinek, *J. Phys.: Condens. Matter* **2017**, 29, 343002.
- [48] E. Artacho, E. Anglada, O. Diéguez, J. D. Gale, A. García, J. Junquera, R. M. Martín, P. Ordejón, J. M. Pruneda, D. Sánchez-Portal, J. M. Soler, *J. Phys.: Condens. Matter* **2008**, 20, 064208.
- [49] A. García, N. Papior, A. Akhtar, E. Artacho, V. Blum, E. Bosoni, P. Brandimarte, M. Brandbyge, J. I. Cerdá, F. Corsetti, R. Cuadrado, V. Dikan, J. Ferrer, J. Gale, P. García-Fernández, V. M. García-Suárez, S. García, G. Huhs, S. Illera, R. Korytár, P. Koval, I. Lebedeva, L. Lin, P. López-Tarifa, S. G. Mayo, S. Mohr, P. Ordejón, A. Postnikov, Y. Pouillon, M. Pruneda, et al., *J. Chem. Phys.* **2020**, 152, 204108.
- [50] J. M. Soler, E. Artacho, J. D. Gale, A. García, J. Junquera, P. Ordejón, D. Sánchez-Portal, *J. Phys.: Condens. Matter* **2002**, 14, 2745.
- [51] N. Papior 2021, <https://doi.org/10.5281/zenodo.597181>.
- [52] I. Horcas, R. Fernández, J. M. Gómez-Rodríguez, J. Colchero, J. Gómez-Herrero, A. M. Baro, *Rev. Sci. Instrum.* **2007**, 78, 013705.